Single-shot readout of the nuclear spin of an on-surface atom

Evert W. Stolte [1,4], Jinwon Lee [1,4] ✉, Hester G. Vennema [1], Rik Broekhoven [1], Esther Teng[1], Allard J. Katan [1], Lukas M. Veldman[2], Philip Willke [3] & Sander Otte [1] ✉

Nuclear spins owe their long-lived magnetic states to their excellent isolation from the environment. At the same time, a finite degree of interaction with their surroundings is necessary for reading and writing the spin state. Therefore, detailed knowledge of and control over the atomic environment of a nuclear spin is key to optimizing conditions for quantum information applications. While various platforms enabled single-shot readout of nuclear spins, their direct environments were either unknown or impossible to controllably modify on the atomic scale. Scanning tunneling microscopy (STM), combined with electron spin resonance (ESR), provides atomic-scale information of individual nuclear spins via the hyperfine interaction. Here, we demonstrate single-shot readout of an individual [49]Ti nuclear spin with an STM. Employing a pulsed measurement scheme, we find its lifetime to be in the order of seconds. Furthermore, we shed light on the pumping and relaxation mechanisms of the nuclear spin by investigating its response to both ESR driving and tunneling current, which is supported by model calculations. These findings give an atomic-scale insight into the nature of nuclear spin relaxation and are relevant for the development of atomically assembled qubit platforms.

Nuclear spins are unique in that they combine subatomic length scales with generally long coherence times. These properties make them appealing candidates for quantum technological applications, while at the same time posing challenges for their readout. Ideally, one would detect the time-dependent behavior of a spin via a single-shot readout, as opposed to a time-averaged measurement. This enables systematically linking specific changes in an open quantum system to observed or controlled changes in its environment, with the potential for real-time feedback. Single-shot readout of individual nuclear spins was achieved in a number of platforms: optically addressed color centers[1–3], molecular break junctions[4], dopants in semiconductors[5,6], and gate-defined quantum dots[7]. While it was shown to be possible to trace the spins in these systems over time with excellent accuracy, their direct environments were either unknown or impossible to controllably modify on the atomic scale.

Spins in individual atoms on surfaces, probed through scanning tunneling microscopy (STM), can be positioned with atomic precision[8]. This allows for engineering the environment, including spin-spin[9] as well as spin-orbit interactions[10,11], and for building desired atomic-scale spin structures for the purpose of atomic-scale quantum simulation experiments[12–14]. Moreover, combining STM with electron spin resonance (ESR)[15] has enhanced the energy resolution and enabled a wealth of detailed studies on composite spin systems[16–20], including their quantum coherent evolution over time[21–23]. Recently, access to the nuclear spin was provided through resolving the hyperfine interaction[24], potentially introducing spins with much longer coherence times to the quantum simulation efforts using atoms on surfaces. While it has been shown that ESR-STM allows for both reading[25,26] and directly driving nuclear spins[27], STM has thus far only sparingly been used to investigate nuclear spins in the time domain[28].

[1]Department of Quantum Nanoscience, Kavli Institute of Nanoscience, Delft University of Technology, Delft, The Netherlands. [2]Institute for Functional Matter and Quantum Technologies, University of Stuttgart, Stuttgart, Germany. [3]Physikalisches Institut, Karlsruhe Institute of Technology, Karlsruhe, Germany. [4]These authors contributed equally: Evert W. Stolte, Jinwon Lee. ✉e-mail: jinwon.lee@tudelft.nl; a.f.otte@tudelft.nl

As such, no nuclear spin lifetimes have yet been reported, and it remains unclear what the dominant relaxation processes are.

In this work, we demonstrate single-shot readout of the nuclear spin state of a single Ti atom, expanding on ESR-STM methodology. We apply a fixed radio frequency (RF), tuned to drive the electron spin if and only if the nuclear spin has magnetization $m_I = -7/2$. If this condition is met, spin-polarized transport through the electron orbital results in a measurable increase in the tunneling current I_{ESR}. We observe that the current switches between its base value I_0 and the increased value $I_0 + I_{ESR}$ on the timescale of seconds. From this, we determine the intrinsic lifetime of the nuclear spin to be 5.3 ± 0.5 s, seven orders of magnitude longer than the lifetime of the electron spin on the same atom[16,22]. In addition, we investigate how the lifetime is affected by the presence of tunneling electrons or a continuous RF signal.

Results and discussion
Single-shot readout
We investigate individual Ti atoms on the oxygen binding site of an MgO/Ag(100) substrate (see "Methods"), which have been shown to carry an electron spin $S = 1/2$ that can be ESR driven by an RF voltage at the STM junction[16], in an external magnetic field oriented out-of-plane. Ti has different isotopes carrying nuclear spins 0, 5/2, or 7/2. In particular, ^{49}Ti has nuclear spin $I = 7/2$ and couples to the electron spin with an out-of-plane hyperfine coupling component $A_\perp = 130$ MHz[28], resulting in a total of 16 energy levels (Fig. 1a). The hyperfine coupling causes a shift in the ESR transition frequency that depends on the nuclear spin state, which is absent for Ti isotopes with $I = 0$ (Fig. 1b, c). The observation of multiple ESR peaks in a single sweep indicates that the nuclear spin state changes much faster than the averaging time of 3 s for each datapoint under conventional ESR settings. The peak heights are a measure of the population distribution of the various nuclear spin states: the nuclear spin resides longer in the $m_I = -7/2$ state as a result of nuclear spin pumping by inelastic electron

scattering[27,28], where m_I refers to the magnetic quantum number of the nuclear spin along the external magnetic field B_z. Being a time-averaged measurement, however, the ESR frequency sweep does not provide information on nuclear spin transition timescales.

In order to resolve changes between the nuclear spin states, we measured the ESR signal in the time domain instead of in the frequency domain. We switched off the STM feedback loop and sent a continuous RF signal to the tunneling junction with a fixed frequency f_{probe}, resonant with a transition of the electron spin magnetic quantum number m_S between states $|m_S,m_I\rangle = |\downarrow, -7/2\rangle$ and $|\uparrow, -7/2\rangle$, resulting in an additional ESR current I_{ESR} only when $m_I = -7/2$, as illustrated in Fig. 1a. Figure 1d shows the current measured for several seconds, revealing stochastic switching between two discrete levels. The two levels become apparent in a histogram of the time trace as two Gaussian distributions separated by a current offset. In contrast, when we use an off-resonance frequency, the current is distributed as a single Gaussian (Supplementary Fig. 1a). We also performed reference measurements on a Ti isotope with $I = 0$ (Supplementary Fig. 1b, c), each revealing a single Gaussian distribution as well. We thus attribute the observed switching to quantum jumps between the probed state ($m_I = -7/2$) and any of the other seven nuclear spin states ($m_I \neq -7/2$).

Since the observed switching time is considerably longer than the averaging time (20 ms), the majority of datapoints constitute a single-shot readout of the nuclear spin. Note that the nuclear spin state is projected at a singular event sometime during the averaging time by an electron passing the adatom. The state is then read out repeatedly during the remaining time to integrate the current to reach a measurable signal strength. This is possible because, in the product state limit, reading out the electron spin state mostly leaves the nuclear spin unchanged after projection. We achieve readout fidelities of up to 98% for both the probed state being occupied and it being unoccupied (see Supplementary Information).

We can probe different nuclear spin states without changing f_{probe} by adjusting the height of the magnetized probe tip, which exerts an
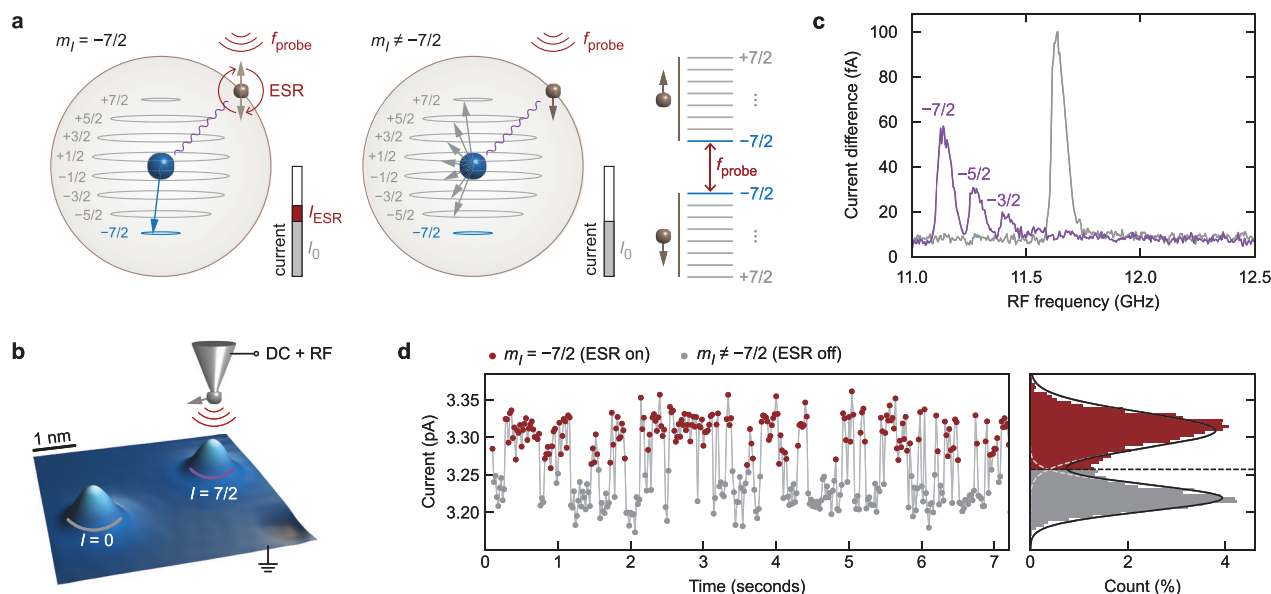
**Fig. 1 | Time-resolved switching of the nuclear spin state. a** Diagram of the measurement scheme: the $I = 7/2$ nuclear spin (blue) of a ^{49}Ti atom coupled to the $S = 1/2$ electron spin (brown) via the hyperfine interaction. Only when the nuclear spin is in the $m_I = -7/2$ state, does the applied RF signal at frequency f_{probe} lead to a tunneling current increase I_{ESR}. Right: spin energy diagram in the limit of a strong magnetic field, where the Zeeman splitting dominates and the eigenstates can be approximated by product states. **b** STM topography (10 pA, 60 mV) of two Ti

isotopes on MgO/Ag(100). **c** ESR frequency sweeps (3.0 pA, 60 mV, $B_z = 1.35$ T, $V_{RF} = 17$ mV, averaging time 3 s, lock-in frequency 270 Hz) measured on the two Ti atoms in (**b**). V_{RF} refers to the zero-to-peak RF voltage amplitude at the tunnel junction. **d** Section of a time trace of the tunneling current at fixed tip height (60 mV, averaging time 20 ms) with f_{probe} corresponding to $m_I = -7/2$. The current histogram on the right is fitted with a two-Gaussian distribution (black line).
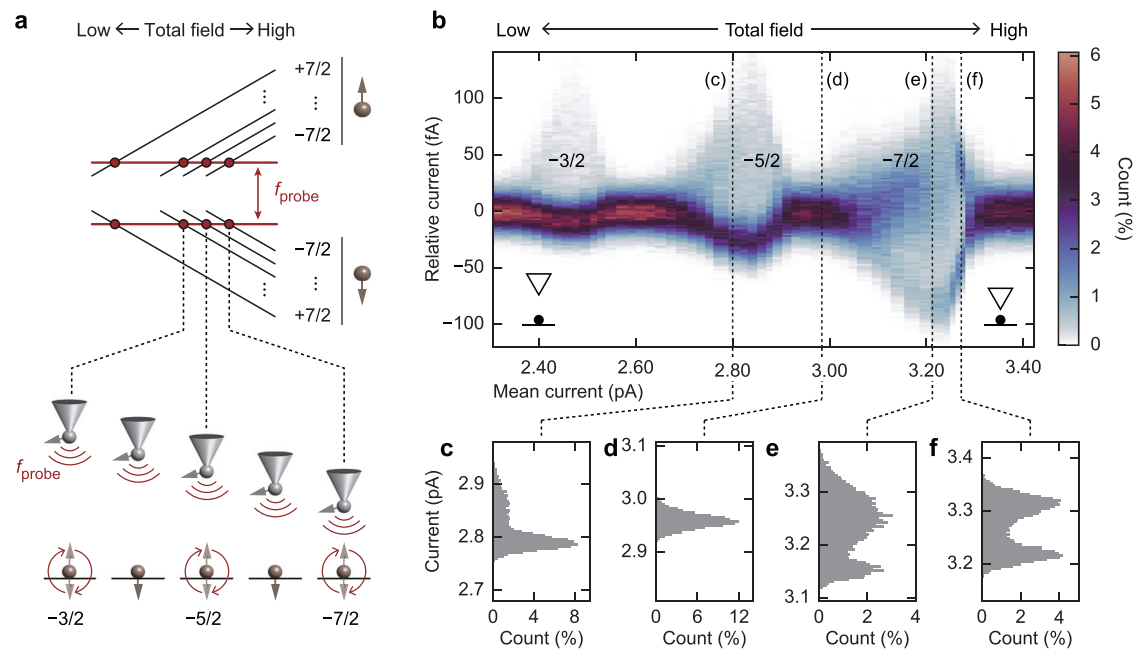
Fig. 2 | Readout of different nuclear spin states. a Energy diagram of the spin states as a function of magnetic field (top) and schematic of the experiment shown in (**b**), indicating that at certain tip heights f_{probe} matches the Zeeman splitting corresponding to one of m_I states (bottom). **b** Color map of current histograms similar to Fig. 1d for different heights of the magnetic STM tip (bias voltage 60 mV). The horizontal axis represents the mean current for each time trace, which is a measure of the total magnetic field. **c**–**f** Current histograms, corresponding to the labeled vertical dashed lines in (**b**).
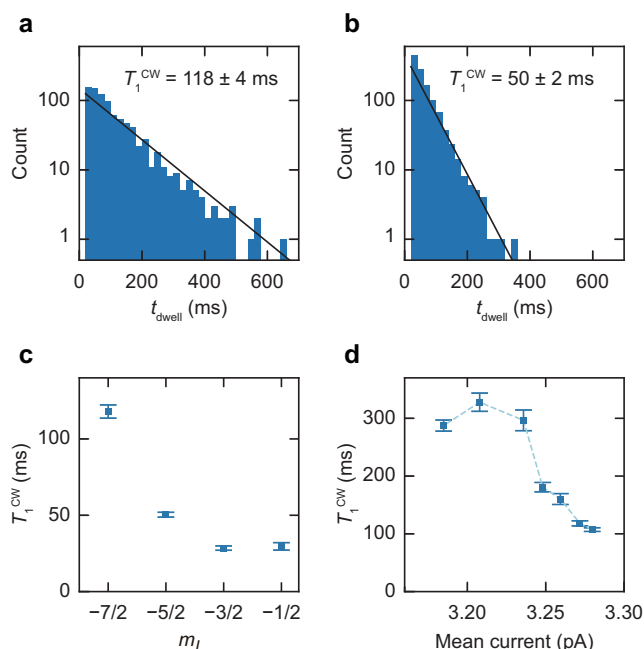
Fig. 3 | Dwell time of different nuclear spin states. a, **b** Histograms of the distribution of the individual dwell times t_{dwell} of $m_I = -7/2$ and $m_I = -5/2$, respectively. Fitting with an exponential function gives the characteristic dwell time T_1^{CW}. Error bars of T_1^{CW} are the standard deviations in the exponential fit parameter. **c** T_1^{CW} for $m_I = -7/2, -5/2, -3/2, -1/2$, applying corresponding f_{probe} at the same tip height. **d** T_1^{CW} of $m_I = -7/2$ at different tip heights around the resonance point.

additional magnetic field on the atom[29]. As we adjust the tip height (i.e., setpoint current), different values of m_I become resonant with f_{probe} (Fig. 2a). We measured current time traces at different tip heights (i.e., different total fields), resulting in a set of current histograms plotted together in Fig. 2b–f. Within the sweep range of the setpoint current, the histograms are found to feature a bimodal distribution in three windows around 3.2, 2.8, and 2.4 pA, matching the resonances of the nuclear spin states $m_I = -7/2$, $-5/2$, and $-3/2$, respectively. While for $m_I = -7/2$ the distribution is ~50–50 (Fig. 2e, f), the other states are found to be occupied much less than half of the time (Fig. 2c).

Lifetime of the nuclear spin

Analysis of the time traces enables us to extract the dwell times of the nuclear spin states. We label each point in the time trace as either in the probed state or not, using a threshold determined by the intersection point of the two Gaussian distributions (Fig. 1d). We measure individual dwell times t_{dwell} for each occurrence of consecutive time spent in the probed state (Fig. 3a). Using an exponential fit, we find a lifetime T_1^{CW} of about 100 ms for $m_I = -7/2$ (Fig. 3a). We note that this is the nuclear spin lifetime under continuous-wave (CW) ESR driving and readout by the tunneling current.

To compare T_1^{CW} between different nuclear spin states, we repeated the experiment for different f_{probe} values while leaving the tip height unchanged to avoid variations in current-induced nuclear spin pumping (Fig. 3b, c, see also Supplementary Fig. 2). We observe that for f_{probe} being resonant with any of the $m_I \neq -7/2$ transitions, T_1^{CW} is significantly shorter than for $m_I = -7/2$. This may be partly attributed to the fact that selection rules allow these states to transition in both directions ($\Delta m_I = \pm 1$), whereas the $m_I = -7/2$ state can only switch to $m_I = -5/2$ ($\Delta m_I = +1$). In addition, these experiments were performed in the presence of a spin-polarized current which constantly excites the system towards $m_I = -7/2$.

However, neither of the above arguments can explain the fact that T_1^{CW} keeps decreasing beyond $m_I = -5/2$, suggesting that the spin pumping efficiency depends on the nuclear spin state. We believe this may be because the hybridization between neighboring spin states depends on m_I directly, which derives from the Clebsch-Gordan coefficients (see Supplementary Table 1). In addition, Fig. 3d shows how T_1^{CW} changes as we vary the tip height around the resonance point for $m_I = -7/2$. We find that T_1^{CW} is increasing further up to ~300 ms as
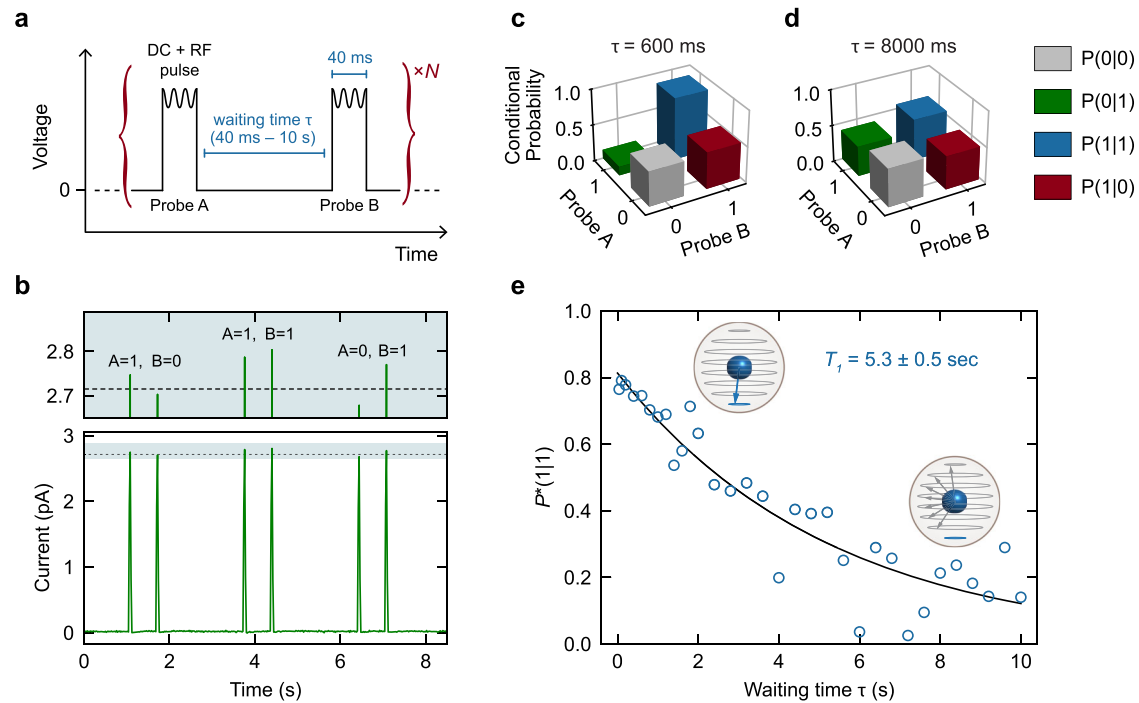
Fig. 4 | Intrinsic nuclear spin lifetime with pulsed detection scheme.
a Schematic of the pulse measurement scheme. One detection event consists of two probe pulses, with a variable waiting time τ in between, with zero bias voltage. Each probe pulse consists of a DC voltage (70 mV) and an RF signal at $f_{probe} = 12.75$ GHz, corresponding to $m_I = -7/2$ ($B_z = 1.6$ T, $V_{RF} = 22.6$ mV). For each τ, we repeat between $N = 443$ and $N = 704$ detection events. **b** Bottom: section of a measured current time trace ($\tau = 600$ ms) showcasing three detection events. Top:

zoom on the shaded area. For each event, the current of the probe pulses A and B indicates whether $m_I = -7/2$ (1) or not (0), based on the current threshold (dashed line) determined from a histogram of all probe pulses. **c, d** Conditional probabilities $P(B|A)$ for $\tau = 600$ ms and $\tau = 8000$ ms, respectively. **e** Corrected conditional probability $P^*(1|1)$ as a function of τ. $P^*(1|1)$ represents the intrinsic decay of the nuclear spin. An exponential fit ($Ae^{-\tau/T_1}$, black curve) gives the intrinsic lifetime T_1 of the $m_I = -7/2$ nuclear spin state ($T_1 = 5.3 \pm 0.5$ s, $A = 0.81 \pm 0.03$).
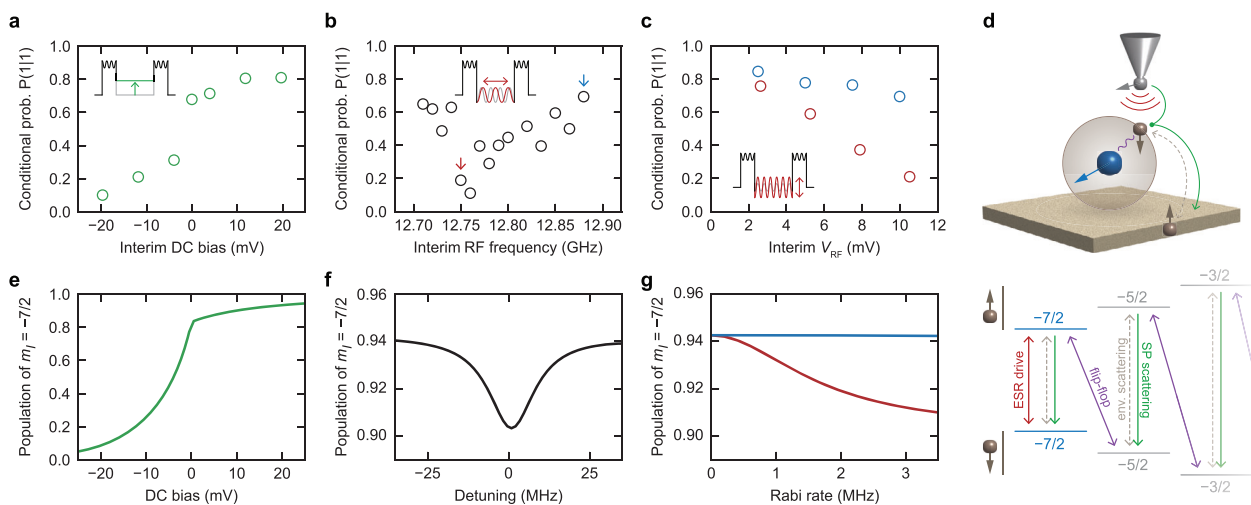
Fig. 5 | DC or RF in the waiting period. a Conditional probability $P(1|1)$ as a function of DC voltage during the waiting section between the two probe pulses (see inset schematic), with a fixed waiting time $\tau = 2$ s. **b** $P(1|1)$ as a function of RF frequency in the waiting section ($\tau = 600$ ms, $V_{RF} = 10.4 \pm 0.3$ mV). **c** Conditional probability $P(1|1)$ as a function of RF voltage amplitude in the waiting section (interim V_{RF}), for two different frequencies highlighted in (**b**) (red: on-resonance frequency, blue: off-resonance frequency). **d** Schematic of the possible transition dynamics between spin states: spin resonance drive of the electron spin (red), flip-flop quantum jump between nuclear and electronic spins mediated by hyperfine coupling (purple), environmental scattering of electronic spin

(gray, dashed), electron spin scattering via spin-polarized STM tip (green).
e–g Rate equation simulations of the experiments performed in (**a**), (**b**), and (**c**), respectively. The model includes all processes indicated in (**d**) and implements them as transition rates between eigenstates. The populations are recorded after time evolution from the initial state $|\downarrow, -7/2\rangle$. Since the simulation does not quantitatively reproduce the experimental unperturbed nuclear lifetime, we chose simulated evolution times to be the same fraction of the simulated lifetime as the experimental ratio τ/T_1 to capture a comparable moment in the decay process (see Supplementary Information).

the system is detuned from resonance. This implies that the continuous ESR driving of the electron spin may affect T_1^{CW} as well.

In order to find the intrinsic lifetime T_1 of the undisturbed nuclear spin and to identify its limiting relaxation mechanisms, we applied a pulsed readout scheme illustrated in Fig. 4a (see "Methods"). Here, we set the voltage (both DC and RF) to zero in between pulses. The probe pulses consisted of similar DC + RF conditions as in the continuous-wave experiments mentioned above. We set the tip height such that f_{probe} matches the resonance frequency for $m_I = -7/2$. As shown in Fig. 4b, the voltage pulses lead to sharp peaks in the current, each of which we can assign either the value 1 (for $m_I = -7/2$) or 0 ($m_I \neq -7/2$), using a threshold as introduced in Fig. 1d. For each pair of probe pulses A and B, there are four possible event scenarios, resulting in conditional probabilities $P(B|A)$ (Fig. 4c, d).

By changing the waiting time τ between the pulses, we then find the conditional probability as a function of τ (Fig. 4e). We take the unintentional pumping of the nuclear spin by the second probe pulse into account, correcting $P(1|1)$ to $P^*(1|1) = [P(1|1) - P(1|0)]/[1 - P(1|0)]$ (see Supplementary Information). $P^*(1|1)(\tau)$ is expected to decrease exponentially as a function of τ due to relaxation processes at a timescale of T_1. By fitting with an exponential function, we obtain $T_1 = 5.3 \pm 0.5$ s for $m_I = -7/2$. Similar measurements on an identical ^{49}Ti atom yielded a value of $T_1 = 4.3 \pm 0.8$ s (Supplementary Fig. 3). This T_1 is seven orders of magnitude larger than the lifetime of the electron spin in the same atom (~100 ns)[16]. In addition, the extracted lifetime is an order of magnitude larger than T_1^{CW} measured in the continuous-wave experiment (Figs. 1 and 2), confirming the hypothesis that the nuclear spin state is affected by continuous ESR driving and DC readout.

Relaxation mechanism

To develop an understanding of how DC spin pumping and ESR driving affect the nuclear spin, we repeat the pulsed experiment introduced in Fig. 4, but now with additional voltages in the waiting time to investigate perturbation of the nuclear spin (Fig. 5a–c) (see "Methods"). In a first variant, we add a DC bias voltage during the waiting phase and fix the waiting time to 2 s. The figure of merit is $P(1|1)$, now left uncorrected by $P(1|0)$ as we intentionally disturb nuclear spins during the waiting time (see Supplementary Information). In Fig. 5a, we plot $P(1|1)$ against the bias voltage in the waiting phase. $P(1|1)$ is found to increase with positive voltage, whereas it decreases with negative voltage.

We attribute this to dynamic nuclear spin polarization resulting from electron spin pumping, which is a combination of two processes depicted in Fig. 5d: flip-flop quantum jumps between a nuclear and electron spin due to hybridization as a result of the hyperfine coupling, and inelastic electron scattering. The former can happen both ways, while the latter is favored in one direction due to the spin polarization of the tip. As a result, the two processes together pump the system towards $m_I = -7/2$ or $m_I = +7/2$, depending on the voltage polarity[27,28].

We note that, since Ti on the oxygen binding site displays a continuous-wave ESR signal only for positive voltages[30], it was previously not possible to observe nuclear spin pumping at negative bias voltage. With our pulsed readout scheme, however, we can now also confirm pumping in this bias regime. This points to an interesting aspect of our experiment compared to previous studies: we isolate the effect of the DC current from the ESR driving, the effect of which will be studied separately below.

In a second and third variant of the experiment, we send an RF signal during the waiting phase and fix the waiting time to 600 ms. In Fig. 5c, d, we change the frequency and RF amplitude, respectively, to see the effect of detuning and ESR driving strength on the conditional probability. During the probe pulses, f_{probe} is kept at 12.75 GHz, corresponding to the $m_I = -7/2$ resonance. As we sweep the interim frequency, $P(1|1)$ dips down on resonance at around 12.75 GHz (Fig. 5b). This is an indication that the nuclear spin relaxes significantly faster when the electron spin is driven most efficiently. As shown in Fig. 5c,

this effect increases with ESR driving amplitude but becomes weaker when the frequency is detuned.

This ESR-induced relaxation can be understood in terms of the availability of the relaxation pathway towards $m_I = -5/2$ via nuclear-electron spin flip-flops. Due to conservation laws, this process can only happen when the electron spin is in the $m_S = \uparrow$ state, whereas $m_S = \downarrow$ is the ground state. The nuclear spin at $m_I = -7/2$ can relax to $m_I = -5/2$ by a hyperfine flip-flop interaction, transferring -1 angular momentum to the electron spin (see Fig. 5d for schematic). Thus, the relaxation rate is amplified when $m_S = \uparrow$ state becomes more populated through ESR driving.

We model the pulsed experiments using rate equation simulations. The model takes into account all interactions visualized in Fig. 5d, including the hybridization due to the hyperfine coupling[27] and an electron spin Rabi drive term. Interestingly, as discussed in the Supplementary Information, the simulation cannot quantitatively reproduce the experimental nuclear lifetime using realistic parameter values. Consequently, we choose to apply the model for qualitative comparison only. The model reproduces the DC pumping behavior (Fig. 5e) and captures the observed dip in the frequency sweep (Fig. 5f) as well as the dependence on driving amplitude (Fig. 5g).

The pulsed experiments together with the simulations provide insight into the relaxation mechanisms limiting the intrinsic lifetime of the nuclear spin. We emphasize that we observed the relaxation by ESR driving to be strong in relation to any other relaxation source present. This indicates that the flip-flop interaction, which facilitates the relaxation by ESR, happens fast enough to be a dominating relaxation process whenever ESR continuously excites the electron spin. We note that the same flip-flop rate is present also when the electron spin is excited in ways other than ESR driving. In thermal equilibrium at 400 mK, electron scattering from the substrate significantly populates the $m_S = \uparrow$ state[31]. We therefore conclude that the nuclear-electron spin flip-flop relaxation channel is likely the main mechanism limiting the intrinsic lifetime.

As the flip-flop interaction results from a small in-plane component of the hyperfine coupling ($A_{\parallel} = 10$ MHz[25]), which in turn depends on the binding site[24], the above implies that the atomic-scale position is a crucial parameter to extend the lifetime of on-surface nuclear spins. Furthermore, the flip-flop relaxation channel is expected to be reduced at higher magnetic fields, where the hybridization is minimized[3]. At that point, other relaxation sources may become relevant, such as spin-lattice coupling mediated by the nuclear quadrupole moment or magnetic Johnson noise from the bulk silver. Dipole-dipole flip-flops with the Mg and Ag nuclear spins can be considered negligible (see Supplementary Note 4).

In conclusion, we performed a single-shot readout of an individual nuclear spin using ESR-STM, which was found to have a lifetime in the order of seconds. Furthermore, we shed light on the pumping channel by a local DC bias and the relaxation channel by ESR driving. As the single-shot readout ESR-STM method presented here should work for any long-lived nuclear spin, the methodology may be transferable to different atomic or molecular spins in various platforms, such as semiconducting or insulating substrates[32,33]. Crucially, the nuclear spin lifetime we observe is longer than the rise time of current amplifiers conventionally used for STM, which enables direct readout and high-fidelity state initialization by projective measurement[34]. Potentially, this could even combine spin operations with STM tip movements between different atoms and open up possibilities to perform simultaneous coherent operations on extended atomic structures comprising multiple spins.

Methods

The experiments were performed in a commercial Unisoku USM-1300 STM. MgO/Ag sample and surface atoms were prepared with the same method described in refs. 21, 28. The tungsten STM tip was

prepared for ESR-STM measurements by first indenting it into the Ag until we obtained scanning image quality, then picking up ~30 Fe atoms. All ESR measurements are taken at a sample temperature of 0.4 K. STM topography was obtained in constant current mode at 1.6 K. All DC bias values are reported with respect to the sample. The pre-amplifier for the tunneling current used for all measurements is the NF corp. SA608F2, with its internal analog 300 Hz low-pass filter active and the NF corp. LP5393 as a low-noise DC power supply for the pre-amplifier.

For CW-mode measurement (Figs. 1–3), we used a Rhode & Schwarz SMA100B signal generator to deliver the RF signal to the STM junction. The DC voltage is generated by a Nanonis V4 Digital-to-Analog converter. During the ESR frequency sweeps, the RF signal was chopped at the frequency of 271 Hz. The ESR signal (difference between driven and non-driven) was detected at this frequency by a Stanford Instruments SR830m lock-in amplifier, resulting in an increased signal-to-noise ratio compared to direct averaging of the current. For the time-trace measurement that resolves nuclear spin state switching, the driving RF voltage is not chopped, and the current is instead recorded directly at a sampling time of 20 ms by a Nanonis V4 Analog-to-Digital converter (ADC). A wiring schematic of the components used for CW-mode measurement is shown in Supplementary Fig. 4a. When recording a CW-mode time trace, we have the RF signal generator running before turning off the tip-height feedback. This provides time for the thermal drift in tip height due to heating to reach an equilibrium to prevent a time-varying drift during the recording.

For pulse-mode measurement (Figs. 4 and 5), the voltage pulses were generated by a Keysight M8195a arbitrary waveform generator (AWG). A single channel was used to generate both the DC and RF voltages directly as one signal. A wiring schematic of the components used for pulse-mode measurement is shown in Supplementary Fig. 4b. In the pulse-mode, the feedback is turned off first before running the AWG, but we start recording after tens of seconds to wait out the drift from heating. The drift settles faster compared to CW-mode due to the short duty cycle of RF pulses. Each section of a signal (probe A, waiting period, probe B, and separation period) is generated by repeating a shorter waveform with a length of 10 μs. It is justified not to have a phase-coherent RF pulse during the probe pulses, because the coherence time of the ESR-driven electron spin is only 300 ns at best[22]. For all pulsed experiments presented with $\tau < 2$ s, the separation period has a length of 2 s. The separation period is equal to the waiting period for longer τ.

Pulsed experiments are recorded at the Nanonis ADC as full-time traces with a sampling rate of 20 ms. A marker signal is sent by the AWG simultaneously with each probe pulse and is recorded at each ADC sample alongside the tunneling current, in order to select the probe pulse samples from all other samples in the time trace for the data analysis. At least 40 ms probe pulse width was chosen to always leave a full 20 ms sample in the center to avoid jitter artifacts at the edges of ADC samples. For details on probe sample selection and subsequent analysis, see Supplementary Information.

Data availability
The raw data generated in this study, as well as the analysis and simulation code, have been deposited in a Zenodo database under the identifier https://doi.org/10.5281/zenodo.15518772.

References

1. Lai, X. Y. et al. Single-shot readout of a nuclear spin in silicon carbide. *Phys. Rev. Lett.* **132**, 180803 (2024).
2. Hesselmeier, E. et al. High-fidelity optical readout of a nuclear-spin qubit in silicon carbide. *Phys. Rev. Lett.* **132**, 180804 (2024).
3. Neumann, P. et al. Single-shot readout of a single nuclear spin. *Science* **329**, 542–544 (2010).
4. Vincent, R., Klyatskaya, S., Ruben, M., Wernsdorfer, W. & Balestro, F. Electronic read-out of a single nuclear spin using a molecular spin transistor. *Nature* **488**, 357–360 (2012).
5. Pla, J. J. et al. High-fidelity readout and control of a nuclear spin qubit in silicon. *Nature* **496**, 334–338 (2013).
6. Asaad, S. et al. Coherent electrical control of a single high-spin nucleus in silicon. *Nature* **579**, 205–209 (2020).
7. Hensen, B. et al. A silicon quantum-dot-coupled nuclear spin qubit. *Nat. Nanotechnol.* **15**, 13–17 (2020).
8. Hirjibehedin, C. F., Lutz, C. P. & Heinrich, A. J. Spin coupling in engineered atomic structures. *Science* **312**, 1021–1024 (2006).
9. Zhou, L. et al. Strength and directionality of surface Ruderman–Kittel–Kasuya–Yosida interaction mapped on the atomic scale. *Nat. Phys.* **6**, 187–191 (2010).
10. Bryant, B., Spinelli, A., Wagenaar, J. J., Gerrits, M. & Otte, A. F. Local control of single atom magnetocrystalline anisotropy. *Phys. Rev. Lett.* **111**, 127203 (2013).
11. Hsueh, Y. L. et al. Engineering spin-orbit interactions in silicon qubits at the atomic-scale. *Adv. Mater.* **36**, e2312736 (2024).
12. Khajetoorians, A. A. et al. Atom-by-atom engineering and magnetometry of tailored nanomagnets. *Nat. Phys.* **8**, 497–503 (2012).
13. Spinelli, A., Bryant, B., Delgado, F., Fernandez-Rossier, J. & Otte, A. F. Imaging of spin waves in atomically designed nanomagnets. *Nat. Mater.* **13**, 782–785 (2014).
14. Toskovic, R. et al. Atomic spin-chain realization of a model for quantum criticality. *Nat. Phys.* **12**, 656–660 (2016).
15. Baumann, S. et al. Electron paramagnetic resonance of individual atoms on a surface. *Science* **350**, 417–420 (2015).
16. Yang, K. et al. Engineering the eigenstates of coupled spin-1/2 atoms on a surface. *Phys. Rev. Lett.* **119**, 227206 (2017).
17. Choi, T. et al. Atomic-scale sensing of the magnetic dipolar field from single atoms. *Nat. Nanotechnol.* **12**, 420–424 (2017).
18. Bae, Y. et al. Enhanced quantum coherence in exchange coupled spins via singlet-triplet transitions. *Sci. Adv.* **4**, eaau4159 (2018).
19. Yang, K. et al. Probing resonating valence bond states in artificial quantum magnets. *Nat. Commun.* **12**, 993 (2021).
20. Wang, H. et al. Construction of topological quantum magnets from atomic spins on surfaces. *Nat. Nanotechnol.* **19**, 1782–1788 (2024).
21. Veldman, L. M. et al. Free coherent evolution of a coupled atomic spin system initialized by electron scattering. *Science* **372**, 964–968 (2021).
22. Wang, Y. et al. An atomic-scale multi-qubit platform. *Science* **382**, 87–92 (2023).
23. Yang, K. et al. Coherent spin manipulation of individual atoms on a surface. *Science* **366**, 509–512 (2019).
24. Willke, P. et al. Hyperfine interaction of individual atoms on a surface. *Science* **362**, 336–339 (2018).
25. Farinacci, L., Veldman, L. M., Willke, P. & Otte, S. Experimental determination of a single atom ground state orbital through hyperfine anisotropy. *Nano Lett.* **22**, 8470–8474 (2022).
26. Kim, J. et al. Anisotropic hyperfine interaction of surface-adsorbed single atoms. *Nano Lett.* **22**, 9766–9772 (2022).
27. Yang, K. et al. Electrically controlled nuclear polarization of individual atoms. *Nat. Nanotechnol.* **13**, 1120–1125 (2018).
28. Veldman, L. M. et al. Coherent spin dynamics between electron and nucleus within a single atom. *Nat. Commun.* **15**, 7951 (2024).
29. Yang, K. et al. Tuning the exchange bias on a single atom from 1 mT to 10 T. *Phys. Rev. Lett.* **122**, 227203 (2019).
30. Kot, P. et al. Electric control of spin transitions at the atomic scale. *Nat. Commun.* **14**, 6612 (2023).
31. Ternes, M. Spin excitations and correlations in scanning tunneling spectroscopy. *New J. Phys.* **17**, 063016 (2015).

32. Sellies, L. et al. Single-molecule electron spin resonance by means of atomic force microscopy. *Nature* **624**, 64–68 (2023).
33. Esat, T. et al. A quantum sensor for atomic-scale electric and magnetic fields. *Nat. Nanotechnol.* **19**, 1466–1471 (2024).
34. Ristè, D., van Leeuwen, J. G., Ku, H. S., Lehnert, K. W. & DiCarlo, L. Initialization by measurement of a superconducting quantum bit circuit. *Phys. Rev. Lett.* **109**, 050507 (2012).

Author contributions
E.W.S., J.L., P.W., and S.O. conceived the experiment. E.W.S. and J.L. performed the experiment. E.W.S., J.L., and E.T. analyzed the experimental data. H.G.V. and R.B. performed the calculations. E.W.S., J.L., H.G.V., R.B., A.J.K., L.M.V., P.W., and S.O. discussed the results. E.W.S., J.L., and S.O. wrote the manuscript, with input from all authors. S.O. supervised the project.

Competing interests
The authors declare no competing interests.

Additional information
Supplementary information The online version contains supplementary material available at https://doi.org/10.1038/s41467-025-63232-5.

Correspondence and requests for materials should be addressed to Jinwon Lee or Sander Otte.

Peer review information *Nature Communications* thanks Yujeong Bae, Stepan Kovarik, and the other, anonymous, reviewer for their contribution to the peer review of this work. A peer review file is available.

Reprints and permissions information is available at http://www.nature.com/reprints

Publisher's note Springer Nature remains neutral with regard to jurisdictional claims in published maps and institutional affiliations.